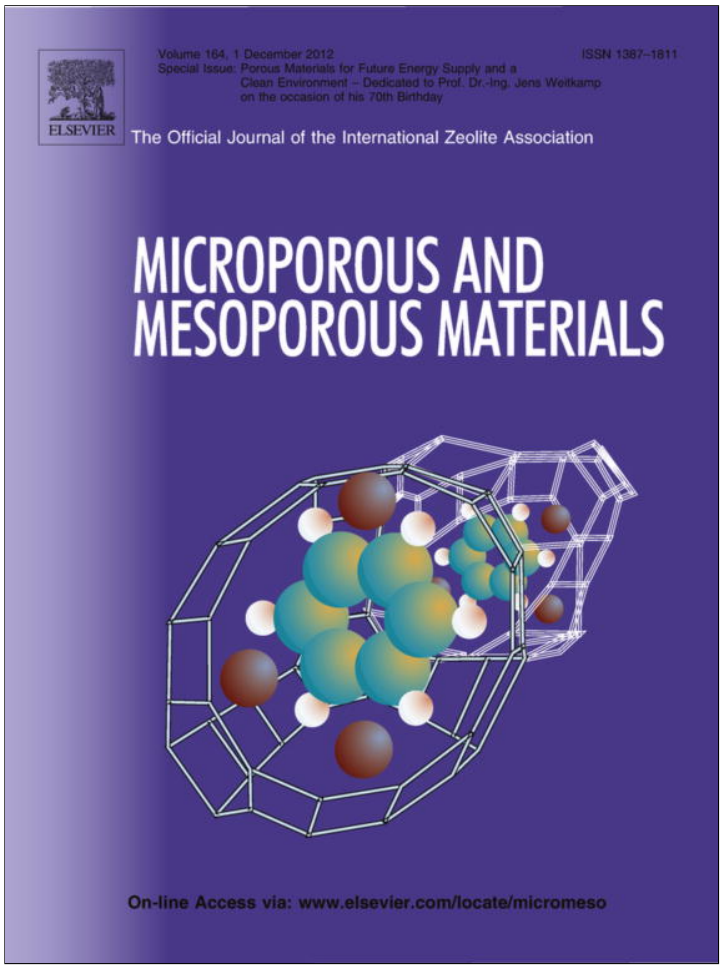

Microporous and Mesoporous Materials 164 (2012) 99–103

Contents lists available at SciVerse ScienceDirect

Microporous and Mesoporous Materials

journal homepage: www.elsevier.com/locate/micromeso

H_2PtCl_6-derived Pt nanoparticles on USY zeolite: A qualitative and quantitative electron tomography study

Jovana Zečević [a], Ad M.J. van der Eerden [a], Heiner Friedrich [b], Petra E. de Jongh [a], Krijn P. de Jong [a,*]

[a] Inorganic Chemistry and Catalysis, Debye Institute for Nanomaterials Science, Utrecht University, Universiteitweg 99, 3584 CG Utrecht, The Netherlands
[b] Laboratory of Materials and Interface Chemistry, Department of Chemical Engineering and Chemistry, Eindhoven University of Technology, Den Dolech 2, 5612 AZ Eindhoven, The Netherlands

ARTICLE INFO

Article history:
Available online 26 June 2012

Keywords:
Zeolite Y
TEM
Electron tomography
Pt/Y
Catalyst synthesis

ABSTRACT

The structural details of a bifunctional Pt/USY catalyst were studied using electron tomography. As a part of a fundamental study on the synthesis of Pt/USY catalyst, H_2PtCl_6 precursor was used for the impregnation of USY zeolite support as a source of negatively charged $PtCl_6^{2-}$ ions in order to restrict interaction with acidic sites of USY zeolite. After heat treatments, it was visualized in 3D that some Pt particles were 3–4 nm in size, while the majority maintained the size of 1.2–1.5 nm which corresponds to the diameter of the zeolite Y micropore cavities (1.2 nm). Electron tomography further revealed that 3–4 nm Pt particles seem to be entrapped in the zeolite crystal, without preferential location in mesopores or at the surface of the crystals. Quantitative image analysis provided the diameters (compared with EXAFS results) and the nearest neighbor distances of hundreds of imaged Pt particles.

1. Introduction

The continuously increasing demand for the improvement of fuel specifications has led to a large number of studies dealing with catalysts that are used in oil refinery processes. In particular bifunctional catalysts, which are commonly employed for hydrocracking and hydrotreating of oil fractions, still receive a great attention. More than two decades ago Weitkamp and others embarked on extensive experimental studies to elucidate hydrocracking reaction mechanism taking place on complex bifunctional catalysts [1–3] which has been nicely summarized in a recent review [4]. Bifunctional catalysts, as the name suggests, combine the two functions of cracking/isomerization brought about by the acid sites of the support and (de)hydrogenation brought about by metal sites deposited on the support. Thus for a catalyst to perform well, it is essential that a balance between the two functions is accomplished [5,6]. In that respect, supported metals should be highly dispersed (i.e. having a high surface-to-volume ratio) and well distributed throughout the support, and in addition be preferably located in the vicinity of the acid sites of the support. Moreover, the porosity of the support has a large influence on the molecular diffusion and hence catalyst performance [7–14].

Pt supported on zeolite Y is an important and industrially relevant example of a bifunctional catalyst. Next to application in hydroisomerization and hydrocracking [11,15,16], Pt and Pd supported zeolite Y catalysts have been recently proposed as possible candidates for hydrodesulfurization [12,13]. Numerous studies have been performed in order to investigate the influence of different heat treatments on Pt dispersion and on the nature of the Pt species [17–22]. $Pt(NH_3)_4^{2+}$ based salts have been found to be the most suitable for impregnations leading to small Pt particles occluded in the zeolite micropores, while negatively charged $PtCl_6^{2-}$ ions are unsuitable since ion-exchange with acidic sites of zeolite would be restricted [23]. In the latter case migration of the weakly adsorbed Pt species is expected, followed by sintering and growth of the Pt particles.

To assess the sizes of the supported Pt particles, bulk techniques are conventionally employed, e.g. CO or H_2-chemisorption or EXAFS, such that the obtained results are an average over $\sim 10^{16}$ particles (as in the case of measuring 100 mg of a 1 wt.% Pt loaded support at 1 nm particle size) [12,18,21,22,24]. Transmission electron microscopy (TEM) is also extensively used to provide local information [18–20,22,24]. However, measuring Pt diameters manually and determining their location from common TEM micrographs is very labor intensive and susceptible to errors due to the overlapping features in 2D projections. To overcome these shortcomings, electron tomography (ET, also referred to as 3D-TEM) has been successfully employed for visualizing the interior/3D morphology of a number of catalysts [11,25–34]. The three-dimensional reconstructions (intensity maps) that are obtained by ET can be subjected to automated image processing which enables quantitative analysis of the catalyst features [30–34]. The advantage of this approach is reflected in a more facile and

* Corresponding author. Tel.: +31 30 253 6762; fax: +31 30 251 1027.
E-mail address: k.p.dejong@uu.nl (K.P. de Jong).

1387-1811/$ - see front matter © 2012 Elsevier Inc. All rights reserved.
http://dx.doi.org/10.1016/j.micromeso.2012.06.024

objective data analysis as compared to time consuming manual measurements.

As a part of broader study on the synthesis of noble metal nanoparticles in zeolites here we use H_2PtCl_6 as a precursor to restrict interaction with acidic sites of USY zeolite and with that enhance the mobility of Pt species. This should further promote migration of Pt from micropores and potentially lead to deposition of Pt in mesopores. The prepared catalyst was submitted to electron tomography and image analysis which enabled a detailed qualitative and quantitative assessment of the Pt properties, including locating Pt particles within the zeolite crystal and determining size distribution as well as distances between Pt particles. The derived average Pt particle sizes were compared with results from EXAFS analysis. Obtaining such detailed structural information on the bifunctional catalyst is crucial to understand the formation mechanism of the desired size and shape of nanoparticles, as well as to understand their catalytic performance which depends not only on the overall dispersion, but also on the location of the active Pt sites.

2. Experimental

2.1. Sample preparation

For this study a commercially available mesoporous USY zeolite (Zeolyst, CBV760) with Si/Al = 30 and in H-form has been used as a support material. Prior to incipient wetness impregnation (IWI), the support was vacuum dried overnight. The appropriate volume and concentration of H_2PtCl_6 aqueous solution was used to impregnate 90% of the zeolite pore volume (determined by N_2-physisorption) in order to achieve 1 wt.% Pt loading of the zeolite. The impregnated powder was dried at 60 °C and 120 °C for 9 h and 10 h, respectively. After drying, the powder was pressed into a tablet, crushed in a mortar and sieved to a 70–40 mesh fraction. The sieved fraction was subsequently transferred to a plug flow reactor and calcined under air flow (~5000 GHSV) at 350 °C for 2 h. The calcination temperature was reached using a heating ramp of 0.5 °C/min. The calcined sample was subsequently submitted to reduction under the flow of H_2/N_2 1/1 mixture (~5000 GHSV), at 600 °C for 3 h in order to further promote the growth of Pt particles. The reduction temperature was reached using a heating ramp of 5 °C/min.

2.2. Characterization

N_2 adsorption and desorption measurement of the pristine zeolite support was performed on a Micromeritics TriStar 3000 at liquid nitrogen temperature. Prior to the measurement, the sample was outgassed in nitrogen flow at 300 °C for 14 h. Micropore and mesopore volumes were obtained using the t-plot and the Barrett–Joyner–Halenda (BJH) method, respectively.

Electron tomography experiments were performed on a Tecnai 20 (FEI) transmission electron microscope operated at 200 kV in bright field imaging mode, while for the common TEM imaging a Tecnai 12 (FEI, 120 kV) was used. Prior to the experiments the Pt/USY powder was suspended in ethanol by sonication, and a few droplets of the suspension were applied on a Quantifoil R2/1 Cu TEM support grid which already contained 5 nm Au particles on top of a thin carbon film. Series of images of Pt/USY particles were acquired over an angular range of ±75° at tilt increments of 2° using a nominal magnification of 29,000 or 50,000 times. Acquired images were aligned to a common origin and rotation axis by tracking the Au particles in IMOD [35]. A stack of finely aligned images was binned by a factor 2 to facilitate further computation and submitted to 3D-reconstruction using a WBP (weighted back projection) algorithm in IMOD. Final reconstructions had a voxel size of $(0.32\ nm)^3$ or $(0.54\ nm)^3$.

Image processing was performed in Matlab using the DipLib toolbox (www.diplib.org). As a first step the 3D-reconstructed volume was processed with a median filter of size 3 in case of Pt segmentation and size 7 in case of zeolite segmentation, in order to reduce noise. The appropriate threshold values were applied on filtered volumes to derive segmented, i.e. binarized volumes of Pt and zeolite. The segmented zeolite volume was submitted to further morphological operations (e.g. dilation, erosion) in order to reduce artifacts originating from the noise, while the Pt segmentation was used without further processing. Segmented zeolite and Pt volumes, as well as Pt particle coordinates were extracted for quantitative analysis. Pt particle size distribution was obtained by calculating the diameters of individual Pt particles from their volume assuming spherical shape. Surface-to-surface distances between nearest neighboring Pt particles were obtained by, first, determining the shortest center-to-center distances based on center of mass coordinates of each Pt particle, followed by subtraction of corresponding radii of the Pt particles to which the shortest distance applies. Pt particles of less than three voxels in diameter were excluded from the analysis on account of sampling limitations. Amira software was used for visualization including volume rendering and isosurface presentations.

The extended X-ray absorption fine structure (EXAFS) Pt L_3 edge measurements were performed at Beamline C of the HASYLAB synchrotron (Hamburg, Germany). The Si(1 1 1) double crystal monochromator was detuned to 50% maximum intensity to reduce the higher harmonics contribution. All measurements were performed in transmission mode where incident and transmitted X-ray beams were detected by ionization chambers filled with a N_2/Ar gas mixture. The gas mixtures were adjusted to absorb 20% of the intensity of the incident beam and 80% of the intensity of the transmitted beam. The beam energy was calibrated by using a platinum foil between the second and third ionization chamber. The appropriate amount of sample, calculated to have a total absorbance of 2.5, was pressed into a self-supporting wafer and placed in a cell operated at atmospheric pressure. Prior to measurement, the pre-reduced sample which had been carefully passivated, was re-reduced in a flow of pure H_2, during heating with 5 °C/min to 200 °C and 20 min at that temperature. Afterwards, the cell was cooled down to room temperature, disconnected from the gas flow with overpressure and cooled down to liquid nitrogen temperature at which the EXAFS measurements were performed.

The absorption data were background subtracted using standard procedures. Data analysis was performed by multiple shell fitting in R-space ($1.5 < R < 3.2$ Å, $2.5 < k < 17$ Å^{-1}, k-weighting 1) using the data analysis package XDAP [36]. The pre-edge background was approximated by a modified Victoreen curve and the post-edge background was subtracted using cubic spline routines. Normalization was performed by dividing the data by the height of the absorption edge at 50 eV. The variances in imaginary and absolute parts were used to determine the fit quality. Further fit quality check is performed by a control calculation with k-weight 3. Different backscatterers were identified by applying the difference-file technique using phase- and amplitude-corrected Fourier transforms. Data for the phase shifts and backscattering amplitudes were obtained from reference compounds. The references were theoretical Pt–Pt and Pt–O references generated by the FEFF7 code and calibrated with experimental spectra of Pt-foil and $Na_2Pt(OH)_6$.

3. Results and discussion

3.1. Textural properties of the pristine support

N_2 adsorption and desorption measurements were performed in order to derive micropore and mesopore volumes of the USY

Table 1
EXAFS results.

Shell	Scatterer	N	$\Delta\sigma^2$ (10^{-3} Å^2)	R (Å)	ΔE_o (eV)
1	Pt	8.26	0.00141	2.766	0.44
2	O	0.33	0.00149	2.085	−10.03

support and, hence, determine the volume of the impregnation solution needed for 90% pore volume filling. A micropore volume of 0.25 cm^3/g was calculated using a t-plot method, while a mesopore volume of 0.20 cm^3/g was obtained from the BJH plot of the adsorption branch. Careful observation of adsorption and desorption isotherms also indicates the presence of some blocked mesopores that can be accessed only through the micropores or through the entrances of less than 3–4 nm diameter. Previous investigations of the pore morphology of the mesoporous USY zeolite had demonstrated in detail the complexity of the mesopore network present within the zeolite crystals [33]. It has been quantitatively shown, using electron tomography and image analysis, that the majority of mesopores is accessible from the outer surface of zeolite crystal through the mesopore network. This is in contrast with earlier tomography study of similar mesoporous USY where it was visually inferred that the blocked type of mesopores dominate [25]. These two opposing conclusions point to variation in textural properties amongst different batches of support material and the necessity for the quantitative approach when analyzing data.

3.2. Bulk Pt/USY sample characterization

Summarized results of the EXAFS measurements are shown in Table 1 and the Fourier transform of the fitted and corresponding data files in both k^1 and k^3 weighting are presented in the Supporting information, Fig. S1. The average Pt–Pt distance is 2.77 Å as expected for larger clusters. The Debye–Waller factor and E_o are small, which is common for cooled samples. The coordination number of 8.26 gives us an average Pt particle size of 1.9 nm when a spherical particle is assumed [37]. The oxygen contribution at a distance of 2.09 Å originates from oxygen in the support. Normally we observe this only with small particles ($\leqslant$1 nm). This suggests a large number of particles of 1 nm or smaller in the micropores, in combination with a substantial number of particles which are larger.

3.3. Local qualitative analysis of Pt/USY morphology

More local information on Pt size and distribution was first derived from TEM imaging. Representative TEM micrographs in Fig. 1 confirm the presence of 3–4 nm Pt particles which seem to be well distributed over the zeolite support (Fig. 1a). At higher magnification and in thinner regions of the zeolite crystals, also 1–2 nm Pt particles can be observed (Fig. 1b). In addition, lighter regions within zeolite crystals reflect the presence of mesopores. The precise measurement of the imaged Pt particles is constrained by the two-dimensional nature of the micrographs where different features along the beam direction appear as overlapping. Hence, it is often hard to discern whether a single Pt particle or two particles on top of each other are imaged (see arrow in Fig. 1a). Moreover, the exact location of Pt particles such as at the zeolite surface, in the mesopores or in the microporous region remains unknown.

To overcome this problem we carried out an electron tomography study which enables the visualization of the catalyst in three dimensions. This is achieved by recording a set of TEM images of a crystal at different tilt angles, which are further used for calculating 3D intensity map, i.e. obtaining a reconstructed volume of the crystal. Fig. 2b shows a 0.32 nm thick cross-section (slice) from the center of a Pt/USY crystal (Fig. 2a). Since the interference of other features from above or below the plane of interest is avoided, the precise location of the Pt particles is obtained. By inspecting the reconstructed volume (Supporting Movie 1, Supporting information), it can be seen that the Pt particles are well distributed throughout the entire zeolite crystal. Interestingly, it seems that Pt particles with sizes larger that the zeolite cages are occluded in the zeolite crystal (Fig. 2b, inset I). This may occur: either by growth followed by local destruction of the crystal lattice or by growth inside small cavity like mesopores, but without pronounced migration into the larger mesopores or to the exterior crystal surface. In addition, small 1–2 nm Pt particles were also successfully resolved (Fig. 2b, inset II). To confirm these findings, we carried out additional ET experiments (Supporting information, Fig. S2). Such a detailed characterization of the morphology is imperative for understanding the catalytic performance, as the reactivity of this bifunctional catalyst depends not only on the overall dispersion but more importantly on the relative locations of both active acid and metal sites.

3.4. Local quantitative analysis of Pt/USY morphology

Even though manual tracing of the Pt particles could be carried out, this process would be very time consuming and susceptible to errors. Therefore automated and operator-independent processing by image analysis is needed to segment and quantify the features of interest. The segmentation procedure, described in detail in Section 2, is schematically presented in the Fig. 3. After applying adequate filters to reduce the noise in the reconstruction, different

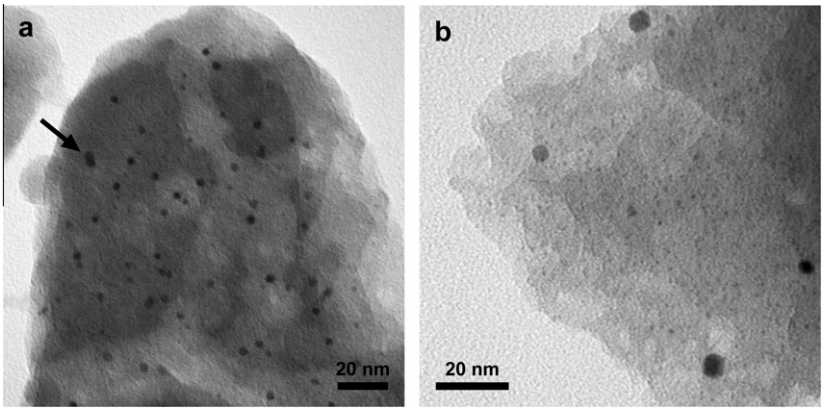

Fig. 1. TEM micrographs of Pt/USY indicating (a) well distributed 3–4 nm Pt particles and (b) presence of small ~1 nm Pt.

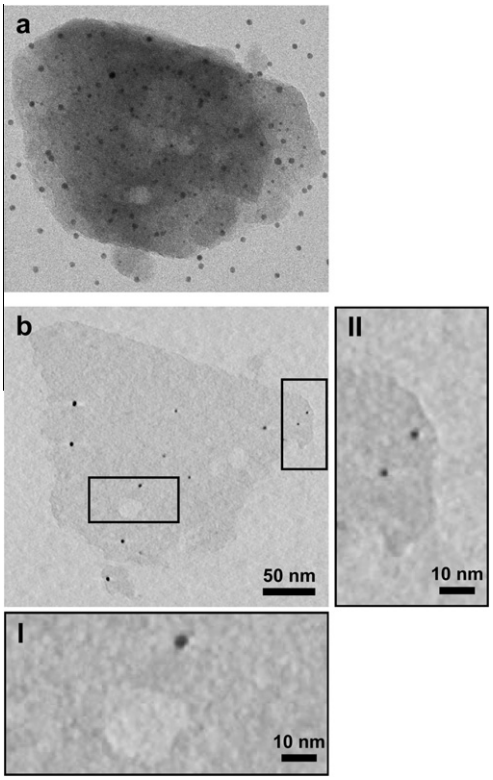

Fig. 2. Electron tomography results. (a) TEM micrograph of Pt/USY crystal at 24° tilt angle; the dark spots in the background are the colloidal gold markers used in the alignment process of the tilt-series and (b) a numerical slice (0.32 nm thick) through the Pt/USY crystal shown in (a), with zoomed-in region I showing an empty mesopore and ~3 nm Pt occluded in the zeolite crystal and region II showing two ~1 nm Pt particles.

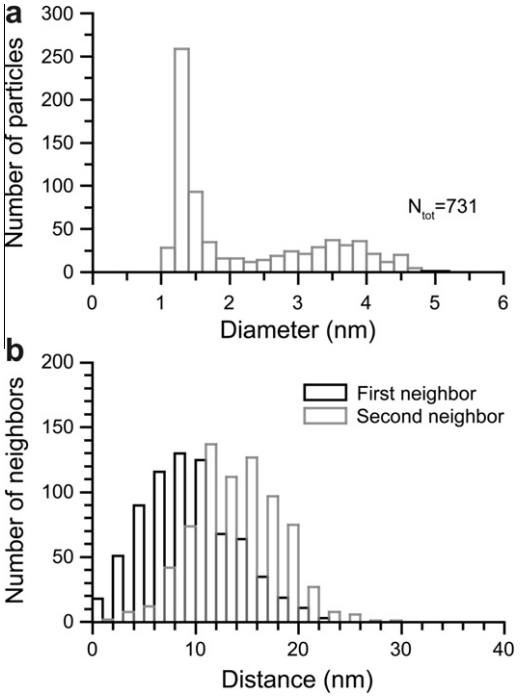

Fig. 4. Quantitative analysis of the segmented Pt particles. (a) Pt particle size distribution and (b) surface-to-surface distances of the first and the second nearest neighboring Pt particles.

threshold values were used in order to segment the Pt particles and the zeolite crystal to derive the volume representation of segmented features (Fig. 3, right). It is important to note that in order to avoid the risk of destructing the zeolite crystal, which would result in movement of the Pt particles during tilt series acquisition, the electron dose was lowered. This resulted in a reduced contrast between the mesopores and zeolite crystal, and a somewhat higher background noise. Nevertheless, hundreds of Pt particles were successfully imaged and segmented and submitted to further quantitative analysis (Fig. 4). From the extracted volumes of all Pt particles, their diameters were calculated assuming a spherical particle shape, and the obtained size distribution curve is shown in Fig. 4a. As can be seen, a bimodal Pt size distribution is present, where small Pt particles of 1.2–1.5 nm in size are most frequent, which corresponds nicely to the 1.2 nm diameter of zeolite Y micropores, and coexist with a wide distribution of larger Pt particles which is centered around 3.5 nm. Such a bimodal distribution was also observed in other crystals (see Supporting information, Fig. S2). This suggests that the Pt was initially well distributed and located inside zeolite micropores, however due to weak adsorption on the zeolite it started to migrate and grow into large particles upon heat treatments. These larger Pt particles can be accommodated in the cavities formed by merging two neighboring

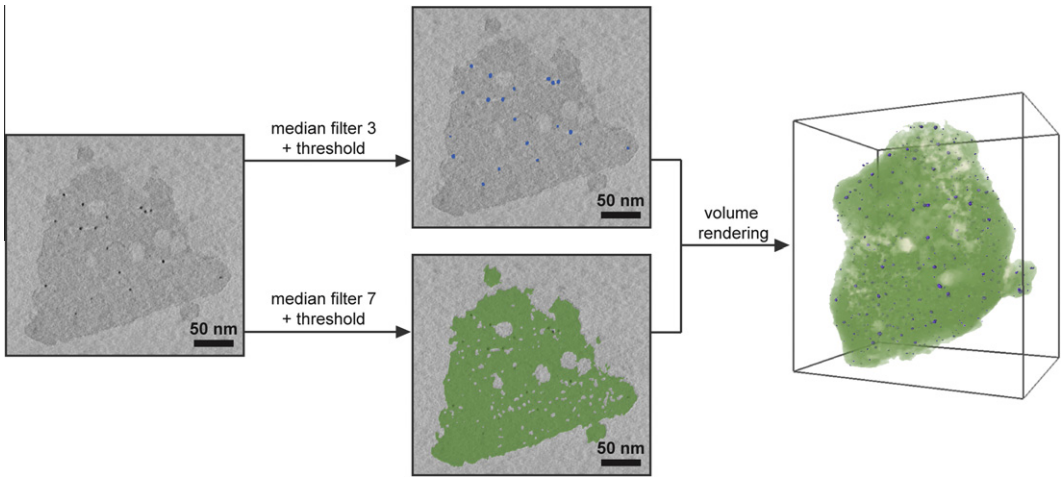

Fig. 3. Illustration of the segmentation process of the Pt particles and the zeolite crystal from the reconstruction. Segmented Pt particles (blue) in the upper middle slice were dilated (grown in diameter) by 2 pixels for better visibility.

supercages of zeolite Y. The characteristic sizes of ~ 3 nm were also observed in an earlier study [11], where base leaching of zeolite Y caused generation of small mesopores in the zeolite crystals. The number-average Pt particle diameter of 2.2 nm obtained by image analysis fits very well with the 1.9 nm derived from EXAFS analysis also considering the bimodal particle size distribution. The slightly lower value obtained by EXAFS may actually indicate the presence of Pt particles even smaller than 1 nm, which were beyond the resolution limit of our ET experiments [34]. Clearly, local analysis by electron tomography and image analysis are of paramount importance for obtaining the actual Pt particle size distribution, which can be misrepresented if only averaged bulk measurements are performed. Furthermore, based on coordinates of each Pt particle, surface-to-surface distances between nearest neighboring particles were calculated (Fig. 4b). Such information is particularly important for studies of particle sintering effects, while the shape of the distance distribution curve also reflects how well particles are distributed over the crystal.

4. Conclusions

The effect of using an "incompatible" $PtCl_6^{2-}$ based precursor for the synthesis of Pt/USY has been studied. Although the interaction of H_2PtCl_6 (aq) with zeolite Y is expected to be weak still very small Pt particles prevail after reduction. Surprisingly, no preference for deposition of Pt in mesopores has been noted suggesting that H_2PtCl_6 did not adsorb there due to alumina enrichment. Electron tomography reveals that part of the weakly adsorbed, and henceforth mobile, Pt species grow into larger (3–4 nm) particles by either migration to small cavity-like mesopores or by locally destroying the zeolite lattice. Remarkably, most of the larger Pt particles seem to be occluded in the zeolite crystal and are inaccessible through the mesopore network. The bimodal particle size distribution points to a preferred size of ~3.5 nm for the larger particles. This diameter coincides with that of two neighboring supercages of zeolite Y and also with the size of small mesopores that emerge upon base leaching of USY zeolite [11]. We speculate that the local properties of the zeolite Y framework favor generation of "defects" of a characteristic size of at least 3 nm. The majority of the Pt particles are 1.2–1.5 nm and present in the micropores, manifesting the importance of zeolite micropores on the stabilization of these particles even when their migration is facilitated by using a weakly adsorbing Pt precursor and high reduction temperatures. In addition, automated image processing and analysis enables easy and more objective measurements when compared to manual processing. This detailed study reveals the potential complexity of bifunctional catalysts and with that emphasizes the need for characterization of local properties in addition to average bulk values.

Acknowledgements

This research was financially supported by Dutch National Research School Combination Catalysis (NRSC-C). The Electron Tomography studies were carried out in the 3D Electron Microscopy group of Utrecht University headed by Dr. Willie Geerts and Dr. Jan Andries Post, with help of Hans Meeldijk. The authors thank the scientific staff at HASYLAB Beamline C (Dr E. Welter) for their interest and stimulating support. Dr. Gonzalo Prieto and Ad Mens are thanked for their involvement in N_2 physisorption measurements.

Appendix A. Supplementary data

Supplementary data associated with this article can be found, in the online version, at http://dx.doi.org/10.1016/j.micromeso.2012.06.024.

References

[1] J. Weitkamp, P.A. Jacobs, J.A. Martens, Appl. Catal. 8 (1983) 123–141.
[2] J.A. Martens, P.A. Jacobs, J. Weitkamp, Appl. Catal. 20 (1986) 239–281.
[3] J.A. Martens, P.A. Jacobs, J. Weitkamp, Appl. Catal. 20 (1986) 283–303.
[4] J. Weitkamp, ChemCatChem 4 (2012) 292–306.
[5] F. Alvarez, F.R. Ribeiro, G. Perot, C. Thomazeau, M. Guisnet, J. Catal. 162 (1996) 179–189.
[6] J.W. Thybaut, C.S.L. Narasimhan, J.F. Denayer, G.V. Baron, P.A. Jacobs, J.A. Martens, G.B. Marin, Ind. Eng. Chem. Res. 44 (2005) 5159–5169.
[7] M. Tromp, J.A. van Bokhoven, M.T. Garriga Oostenbrink, J.H. Bitter, K.P. de Jong, D.C. Koningsberger, J. Catal. 190 (2000) 209–214.
[8] P. Kortunov, S. Vasenkov, J. Kärger, R. Valiullin, P. Gottschalk, M. Fé Elía, M. Perez, M. Stöcker, B. Drescher, G. McElhiney, C. Berger, R. Gläser, J. Weitkamp, J. Am. Chem. Soc. 127 (2005) 13055–13059.
[9] Y. Sun, R. Prins, Angew. Chem., Int. Ed. 47 (2008) 8478–8481.
[10] Y. Sun, H. Wang, R. Prins, Catal. Today 150 (2010) 213–217.
[11] K.P. de Jong, J. Zečević, H. Friedrich, P.E. de Jongh, M. Bulut, S. van Donk, R. Kenmogne, A. Finiels, V. Hulea, F. Fajula, Angew. Chem., Int. Ed. 49 (2010) 10074–10078.
[12] W. Fu, L. Zhang, T. Tang, Q. Ke, S. Wang, J. Hu, G. Fang, J. Li, F.-S. Xiao, J. Am. Chem. Soc. 133 (2011) 15346–15349.
[13] L. Zhang, W. Fu, Q. Ke, S. Zhang, H. Jin, J. Hu, S. Wang, T. Tang, Appl. Catal. A. http://dx.doi.org/10.1016/j.apcata.2012.05.028.
[14] D. Verboekend, G. Vilé, J. Pérez-Ramírez, Adv. Funct. Mater. 22 (2012) 916–928.
[15] J.F.M. Denayer, J.A. Martens, P.A. Jacobs, J.W. Thybaut, G.B. Marin, G.V. Baron, Appl. Catal. A Gen. 246 (2003) 17–28.
[16] G. Burnens, C. Bouchy, E. Guillon, J.A. Martens, J. Catal. 282 (2011) 145–154.
[17] P. Gallezot, A. Alarcon-Diaz, J.-A. Dalmon, A.J. Renouprez, B. Imelik, J. Catal. 39 (1975) 334–349.
[18] M.S. Tzou, B.K. Teo, W.M.H. Sachtler, J. Catal. 113 (1988) 220–235.
[19] M. Pan, J.M. Cowley, I.Y. Chan, Catal. Lett. 5 (1990) 1–12.
[20] B.F. Chmelka, G.T. Went, R. Csencsits, A.T. Bell, E.E. Petersen, C.J. Radke, J. Catal. 144 (1993) 506–524.
[21] K.I. Pandya, S.M. Heald, J.A. Hriljac, L. Petrakis, J. Fraissard, J. Phys. Chem. 100 (1996) 5070–5077.
[22] J. de Graaf, A.J. van Dillen, K.P. de Jong, D.C. Koningsberger, J. Catal. 203 (2001) 307–321.
[23] J.R. Regalbuto, in: K.P. de Jong (Ed.), Synthesis of Solid Catalysts, Wiley-VCH Verlag GmbH & Co. KGaA, Weinheim, 2009, pp. 33–58.
[24] Y. Ji, A.M.J. van der Eerden, V. Koot, P.J. Kooyman, J.D. Meeldijk, B.M. Weckhuysen, D.C. Koningsberger, J. Catal. 234 (2005) 376–384.
[25] A.H. Janssen, A.J. Koster, K.P. de Jong, Angew. Chem. Int. Ed. 40 (2001) 1102–1104.
[26] P.A. Midgley, E.P.W. Ward, A.B. Hungría, J.M. Thomas, Chem. Soc. Rev. 36 (2007) 1477–1494.
[27] H. Friedrich, P.E. de Jongh, A.J. Verkleij, K.P. de Jong, Chem. Rev. 109 (2009) 1613–1629.
[28] O. Ersen, J. Werckmann, M. Houllé, M.-J. Ledoux, C. Pham-Huu, Nano Lett. 7 (2007) 1898–1907.
[29] J.C. González, J.C. Hernández, M. López-Haro, E. del Río, J.J. Delgado, A.B. Hungría, S. Trasobares, S. Bernal, P.A. Midgley, J.J. Calvino, Angew. Chem., Int. Ed. 48 (2009) 5313–5315.
[30] C.J. Gommes, K.P. de Jong, J.-P. Pirard, S. Blacher, Langmuir 21 (2005) 12378–12385.
[31] H. Friedrich, C.J. Gommes, K. Overgaag, J.D. Meeldijk, W.H. Evers, B. de Nijs, M.P. Boneschanscher, P.E. de Jongh, A.J. Verkleij, K.P. de Jong, A. van Blaaderen, D. Vanmaekelbergh, Nano Lett. 9 (2009) 2719–2724.
[32] R. Grothausmann, G. Zehl, I. Manke, S. Fiechter, P. Bogdanoff, I. Dorbandt, A. Kupsch, A. Lange, M.P. Hentschel, G. Schumacher, J. Banhart, J. Am. Chem. Soc. 133 (2011) 18161–18171.
[33] J. Zečević, C.J. Gommes, H. Friedrich, P.E. de Jongh, K.P. de Jong, Angew. Chem., Int. Ed. 51 (2012) 4213–4217.
[34] H. Friedrich, S. Guo, P.E. de Jongh, X. Pan, X. Bao, K.P. de Jong, ChemSusChem 4 (2011) 957–963.
[35] J.R. Kremer, D.N. Mastronarde, J.R. McIntosh, J. Struct. Biol. 116 (1996) 71–76.
[36] M. Vaarkamp, J.C. Linders, D.C. Koningsberger, Physics B 209 (1995) 159–160.
[37] A. Jentys, Phys. Chem. Chem. Phys. 1 (1999) 4059–4063.